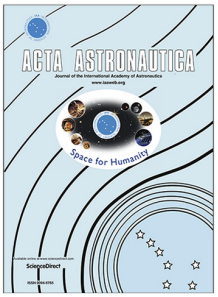
Journal Pre-proof



Magnetic confinement of a heaterless hollow cathode plasma in an applied-field MPD thruster configuration

Jakob Balkenhohl, Nicholas Rattenbury, John Cater

PII: S0094-5765(26)00753-8
DOI: https://doi.org/10.1016/j.actaastro.2026.11.001
Reference: AA 12374

To appear in: *Acta Astronautica*

Received date : 9 March 2026
Revised date : 16 October 2026
Accepted date : 1 November 2026

Please cite this article as: J. Balkenhohl, N. Rattenbury and J. Cater, Magnetic confinement of a heaterless hollow cathode plasma in an applied-field MPD thruster configuration, *Acta Astronautica* (2026), doi: https://doi.org/10.1016/j.actaastro.2026.11.001.

This is a PDF of an article that has undergone enhancements after acceptance, such as the addition of a cover page and metadata, and formatting for readability. This version will undergo additional copyediting, typesetting and review before it is published in its final form. As such, this version is no longer the Accepted Manuscript, but it is not yet the definitive Version of Record; we are providing this early version to give early visibility of the article. Please note that Elsevier's sharing policy for the Published Journal Article applies to this version, see: https://www.elsevier.com/about/policies-and-standards/sharing#4-published-journal-article. Please also note that, during the production process, errors may be discovered which could affect the content, and all legal disclaimers that apply to the journal pertain.

© 2026 Published by Elsevier Ltd on behalf of IAA.

Revised manuscript (unmarked, editable source file) Journal Pre-proof Click here to view linked References

Magnetic Confinement of a Heaterless Hollow Cathode Plasma in an Applied-Field MPD Thruster Configuration

Jakob Balkenhohl[a,*], Nicholas Rattenbury[a], John Cater[b]

[a] *Te Pūnaha Ātea – Space Institute, The University of Auckland, Auckland, 1010, New Zealand*
[b] *Auckland University of Technology, Auckland, 1010, New Zealand*

Abstract

A spatially resolved experimental investigation was conducted on a heaterless thermionic hollow cathode discharge operated in an enclosed, magnetically confined geometry representative of a low-power applied-field magnetoplasmadynamic (AF-MPD) thruster. Axial magnetic fields of up to 800 G were applied while maintaining discharge currents below 10 A in argon. Langmuir, emissive, and retarding potential analyser diagnostics were used to obtain electron energy probability functions (EEPFs), plasma potentials, and ion energy distribution functions (IEDFs) throughout the near-field and expanding plume. Increasing magnetic field strength produced a transition from a diffuse, weakly ionised discharge to a highly confined plasma jet exhibiting on-axis densities nearly two orders of magnitude higher and electron temperatures approaching 9 eV. Plasma potential maps revealed the formation of a nozzle-like electrostatic structure that directed ions axially and radially inward, promoting on-axis acceleration. Corresponding IEDF measurements confirmed the emergence of a magnetically enhanced ion beam, with beam current increasing strongly with field strength at approximately constant beam energy. The combined results demonstrate that strong axial magnetic confinement fundamentally alters both electron and ion transport in low-power hollow-cathode discharges, supporting the use of heaterless hollow cathodes as plasma injectors for compact AF-MPD thrusters.

Keywords: Hollow cathode, Plasma diagnostics, Applied-Field MPD thruster, Magnetic confinement, Electron energy distribution

1. Introduction

Applied-field magnetoplasmadynamic (AF-MPD) thrusters have been recognised for their ability to generate high thrust densities by coupling electromagnetic and electrostatic acceleration within a quasi-neutral plasma [1, 2]. Historically, the large discharge currents required for self-field operation restricted these systems to high-power regimes, where high efficiency is offset by considerable power and mass demands [3, 4]. However, advances in compact, high-temperature-superconducting (HTS) magnet technology and space-qualified cryocoolers now enable the generation

*Corresponding author
Email address: jakob.balkenhohl@gmail.com (Jakob Balkenhohl)

Journal Pre-proof

Journal Pre-proof

of strong axial magnetic fields at substantially lower power levels [5]. This progress has renewed interest in low-power AF-MPDT architectures capable of operating below 10 kW with applied fields exceeding several hundred milliTesla [6], offering an attractive route toward scalable, magnetically controlled plasma propulsion.

A critical challenge in this emerging regime is maintaining stable plasma generation and efficient current transfer when discharge currents fall below approximately 10 A. Conventional rod cathodes, long employed in MPD configurations, exhibit poor ionisation efficiency and unstable attachment at low current densities [7, 8]. In contrast, thermionic hollow cathodes (HCs) provide dense, low-voltage plasmas and have demonstrated reliability as electron sources in Hall and ion thrusters [9, 10]. Their potential as on-axis plasma injectors in AF-MPDTs is therefore compelling, particularly where magnetic confinement can mitigate plume divergence and enhance ion acceleration. However, systematic investigations of hollow cathodes operating within enclosed, strongly magnetised geometries remain scarce, and little is known about how such fields modify local plasma transport and energy conversion. Existing work includes studies of magnetically influenced hollow cathode discharges in Hall and ion thruster contexts [11–13], but these differ substantially in geometry, power level, and field strength from the AF-MPDT relevant regime explored here.

The present study addresses this gap experimentally by characterising a heaterless thermionic hollow cathode operating within an AF-MPDT-like configuration under axial magnetic fields up to 800 G. Using spatially resolved Langmuir, emissive, and retarding potential analyser diagnostics, we examine how magnetic confinement alters the electron energy probability function (EEPF), electron density, electron temperature, plasma potential, and ion energy distribution across the near-field and expanding plume. Particular emphasis is placed on identifying the mechanisms responsible for beam formation and axial acceleration, as well as evaluating the implications for thrust generation and cathode-based plasma injection.

The results presented represent, to the authors' knowledge, the first fully spatially resolved kinetic characterisation of a heaterless hollow-cathode discharge in a magnetically confined, AF-MPDT relevant geometry. These provide new insight into the coupling between magnetic confinement, electron heating, and ion acceleration, with direct implications for the design of compact, low-power magnetoplasmadynamic propulsion systems.

2. Experimental Apparatus and Diagnostics

Experiments were conducted in the *Kākāpō* facility at the University of Auckland, a custom-built vacuum platform designed to investigate hollow cathode plasmas under axial magnetic confinement in an AF-MPDT configuration [14]. The stainless-steel chamber has an internal diameter of 0.5 m and length of 1 m, and is evacuated to a base pressure of 1×10^{-7} Torr using a turbomolecular pump backed by a roughing pump. During operation with argon flows of 5 sccm to 15 sccm, the chamber pressure remained below 0.8 mTorr, ensuring a collisional environment representative of near-field MPDT conditions while limiting background ionisation. All components were mounted on a grounded aluminium breadboard with alumina insulation where required. Optical access was provided by a KF-40 viewport and an internal camera for plume imaging.

Journal Pre-proof

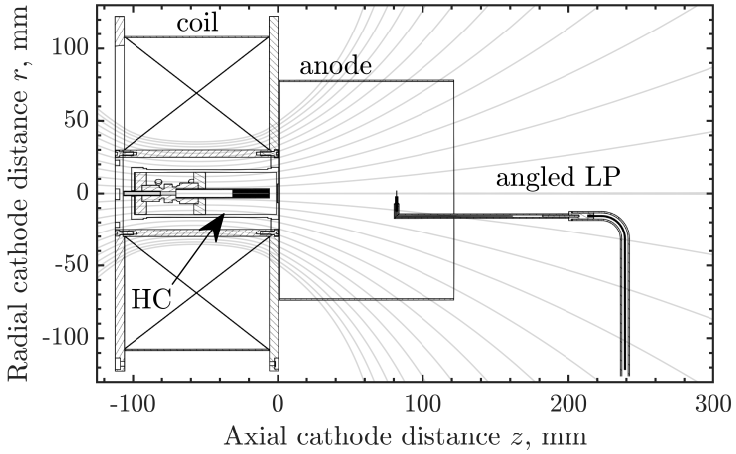


Figure 1: A simplified to-scale schematic of the experimental apparatus showing its main components, the magnetic field lines, and the r–z coordinate system used for spatial plume measurements. HC denotes the hollow cathode and LP the Langmuir probe.

2.1. Hollow Cathode and Discharge Circuit

The plasma source was a heaterless thermionic hollow cathode using a Kaufman & Robinson tantalum emitter and keeper assembly. A 150 mm inner-diameter cylindrical anode enclosed the cathode, with a fixed keeper–anode spacing of 0 mm and an anode length of 120 mm (see Fig. 1). This geometry was selected to match the enclosed, injection-like configuration expected in low-power AF-MPDT operation. The term heaterless refers to the ignition mode: no external resistive heater is employed. Instead, the tantalum insert is self-heated by ion bombardment and resistive dissipation during the keeper discharge, after which thermionic emission from the insert sustains the main plasma. The term thermionic distinguishes the emission mechanism from photoemission or field emission.

Ignition was provided by a 1000 V, 2 A supply connected to the keeper. A series 110 Ω potentiometer limited current surges during breakdown. The main discharge was driven by a 200 V, 15 A supply connected to the anode, with the cathode tube and negative terminals referenced to chamber ground. Anode and keeper voltages (V_A, V_K) were measured using 10:1 passive probes (2.5 kV rating), and currents (I_A, I_K) were recorded via shunt resistors. All signals were sampled at 200 kHz.

2.2. Magnetic Field System

Axial magnetic fields were generated using a custom solenoid with a 50 mm inner diameter, centred on the cathode such that the keeper head was flush with the coil bobbin. The coil, powered by a 12 kW supply, provided up to 32 A corresponding to peak axial fields of 6120 G. Throughout this work, magnetic field strengths B refer to the maximum on-axis value $B_{z,\mathrm{max}}$. The axial field profile is shown in Fig. 5a.

2.3. Plasma Diagnostics

Three complementary diagnostics were constructed and employed to characterise the electron energy distribution, plasma potential, and ion energy distribution.

Journal Pre-proof

Langmuir probe. A single swept Langmuir probe with a 127μm diameter, 3 mm long tungsten tip acquired current–voltage characteristics over -60 to +60 V. A custom analogue differentiator delivered the first and second derivatives in real time, enabling direct EEPF extraction without numerical noise amplification. Electron number density n_e and effective temperature $T_\mathrm{e,eff}$ were computed from the EEPF via Druyvesteyn analysis [15]. An angled design was implemented to ensure perpendicularity of the probe tip with respect to the magnetic field lines and to enable measurement within the anode (see Fig. 1).

The Druyvesteyn second-derivative method used to extract EEPFs assumes an isotropic, collisionless velocity distribution within the probe sheath. Collisionlessness is satisfied throughout the measurement domain: at background pressures of 0.5–0.8 mTorr, the electron–neutral mean free path is of order metres, far exceeding both the probe sheath scale ($\sim \lambda_\mathrm{D}$, 50–200 μm) and the spatial extent of the measurement grid. Quasi-neutrality holds at all measurement locations ($\lambda_\mathrm{D}/L_\mathrm{n} \ll 1$). The condition $r_\mathrm{p} \ll r_\mathrm{L,e}$ is satisfied at all field strengths and positions. Here $B_{z,\max}$ is the peak on-axis value at the coil centre; the field sampled by the probe is considerably lower, since the on-axis profile decays with distance from the coil (Fig. 5a) and thermal loading restricts the strongest case to $z \geq 10$ cm. At that nearest accessible position the local on-axis field is ~ 50 G, giving $r_\mathrm{L,e} \geq 0.7$ mm at $T_\mathrm{e} = 2$ eV, still far larger than $r_\mathrm{p} = 64\,\mu$m. The probe is therefore effectively unmagnetised and the full cylindrical collection area is appropriate [16]. The probe tip was oriented perpendicular to the magnetic field at all positions to maintain a constant effective collection area and prevent depletion of field-line-trapped electrons. Each measurement was averaged over 100 voltage sweeps at 20 Hz and binned at 0.1 V resolution. The discharge was operated at 3 A, well below the tens of amperes at which the most energetic hollow cathode oscillations have been reported, and at less than one-third of the cathode's 10 A design current, placing it in a lightly loaded regime not typically associated with plume-mode onset.

EEPF-derived plasma parameters were validated at each measurement location against two independent checks:

1. the plasma potential extracted from the I'' zero-crossing was compared against the emissive probe measurement and retained only where agreement was within ± 2 V; and
2. the low-energy gap $\delta\varepsilon$ in the raw EEPF was screened against an empirically established operational threshold, rather than a derived physical constant, below which the Druyvesteyn reconstruction is reliable.

Measurements passing both checks were further supported by comparison of the EEDF-integrated density, $n_{e,\mathrm{EEDF}}$, against the orbital-motion-limited electron saturation density, $n_{e,\mathrm{OML}}$, with the OML agreement embedded directly in the uncertainty via the confidence factor

$$\gamma = 1 - \left| \frac{n_{e,\mathrm{EEDF}} - n_{e,\mathrm{OML}}}{n_{e,\mathrm{OML}}} \right|,$$

which was included in the quadrature uncertainty sum. Measurements failing either the ± 2 V potential check or the gap screen were excluded. Representative raw I–V

Journal Pre-proof

characteristics and their analogue-derived second derivative are provided in the supplementary material (Fig. S1) for all five principal field strengths.

Emissive probe. A tungsten emissive probe was operated using the floating-potential method, in which the filament heating current was gradually increased while the probe floating potential was recorded, and the plasma potential was taken at the knee of the resulting curve. Depending on local plasma conditions, electron emission became significant above heating currents of approximately 2–3 A (the emission current itself is not measured directly in floating mode). Repeated measurements at a fixed location varied by less than ±0.5 V, and the results agreed with the Langmuir-probe plasma potential to within 2 V across the operating conditions investigated. Unlike the Langmuir probe, the emissive probe is not subject to distortion from time-averaging over a nonlinear I–V characteristic, and therefore provides an independent cross-check of the time-averaged plasma potential unaffected by the second-derivative averaging artefact discussed in Sec. 4.1.

Retarding potential analyser (RPA). A four-grid planar RPA aligned with the plume axis measured the ion current as a function of retarding voltage with a resolution of approximately 0.5 eV. The grids used a 55 % transparency nickel mesh, with grid spacing designed against the smallest measured Debye length (∼50 μm) to ensure adequate ion transmission and sheath resolution. From these measurements, ion energy distribution functions (IEDFs), ion beam currents, and beam potentials were extracted. Due to probe size and current limitations, measurements were acquired along the central axis between $z = 15$ cm and 27 cm. IEDFs were obtained by differentiating the I_C–V_D characteristic using the same analogue differentiator circuit, with 200 sweeps averaged at 20 Hz. Overlapping beam and bulk populations were separated using a Gaussian deconvolution procedure. The uncertainty in the extracted beam potential, V_B, is ±2 V based on the fit residuals, propagating to an uncertainty in the beam velocity,

$$v_b = \sqrt{\frac{2e(V_B - V_p)}{m_{\mathrm{Ar}}}},$$

of approximately ±900 m/s via Gaussian error propagation:

$$\sigma_{v_b} = \left(\frac{e}{2m_{\mathrm{Ar}}\Delta V}\right)^{1/2} \sqrt{\sigma_{V_B}^2 + \sigma_{V_p}^2},$$

where

$$\Delta V = V_B - V_p \approx 10\text{–}15\,\mathrm{V}, \qquad \text{and} \qquad \sigma_{V_B} = \sigma_{V_p} = 2\,\mathrm{V}\,.$$

All probes were mounted on a custom-built two-axis translation stage referenced to the cathode orifice plane, as shown in Fig. 1. Automated mapping covered a 290 × 120 mm area centred on the axis with a 5 mm grid spacing. Each measurement plane was mirrored about r = 0 to reconstruct a full r–z field while minimising probe intrusion. Consistency checks at the start and end of each map verified stationarity of the discharge and any data sets exhibiting drift were repeated. Data acquisition and stage control were integrated in LabVIEW, which coordinated sweep timing, probe motion, and power supply set-points.

Journal Pre-proof

3. Operating Conditions and Baseline Characterisation

To establish a reference framework for the spatially resolved diagnostics presented later, the hollow cathode discharge was characterised over a range of anode currents, mass flow rates, and applied magnetic field strengths. Particular emphasis was placed on understanding how axial confinement affects global electrical behaviour and plume structure, as these features govern the subsequent evolution of the electron and ion populations.

3.1. Discharge Response to Applied Magnetic Field

The anode voltage V_A was recorded as a function of the maximum axial magnetic field $B_{z,\max}$ for anode currents between 1 – 5 A and mass flow rates of 5, 10, and 15 sccm. The resulting trends are shown in Fig. 2. At $B = 0$, the discharge follows typical thermionic hollow-cathode behaviour, with the voltage decreasing as the anode current increases until a minimum is reached, followed by a gradual rise at higher currents [9, 17].

The application of even a weak axial magnetic field results in an increase in the anode voltage regardless of the set anode current or mass flow rate. This behaviour is consistent with inhibited cross-field electron transport. In the present cathode–anode–magnet geometry, the outermost field line intersecting the cathode orifice does not connect to the anode; electrons must therefore diffuse across magnetic field lines to reach the anode. Increasing B enhances radial confinement and suppresses this diffusion, requiring a higher potential drop to maintain a fixed discharge current. The estimated electron gyroradii at low field ($B \approx 9$ G) are already well below the 75 mm anode radius, indicating that electrons are magnetised throughout the entire operational range.

The voltage–field dependence is strongly non-linear and sensitive to mass flow rate. At fixed I_A, higher mass flow rate $\dot{m}$ generally lowers the anode voltage due to increased collisionality, however Fig. 2 illustrates that the detailed behaviour depends on flow rate. For $\dot{m} = 15$ sccm, a pronounced local maximum occurs near $B \approx 250$ G, producing higher voltages than at lower flow rates despite the greater neutral density. This non-monotonicity suggests that magnetic confinement modifies both the density distribution and ionisation balance in the near-cathode region.

Discharge stability was evaluated via the relative standard deviation of the anode voltage, plotted in Fig. 2(d–f). At low fields, the sharp rise in V_A coincides with a reduction in fluctuations, indicating initial stabilisation. As the field increases further, fluctuations increase again, with the onset depending on both mass flow rate and current. The maximum relative variation observed was approximately 4 %, remaining below the typical ∼10 % threshold indicative of a transition to plume mode [18]. Thus, although high-field operation introduces low-level magnetised instabilities, the discharge remains comparatively quiescent across the accessed parameter space.

At sufficiently high magnetic fields, discharge operation becomes limited by the onset of arcing between the anode and grounded chamber surfaces. Enhanced magnetic confinement leads to downstream charge accumulation, raising the plasma potential relative to ground, as reflected by the systematic increase in measured plasma and anode potentials with increasing B. This behaviour can be interpreted

using the simplified equivalent circuit shown in Fig. 3, in which the confined cathode–anode plasma column is represented by an effective impedance R_{p1}, in parallel with an alternate conduction path to the grounded chamber walls with impedance R_{p2}. As magnetic confinement increases, the effective impedance of the main plasma column rises due to inhibited cross-field transport, while the downstream plasma potential

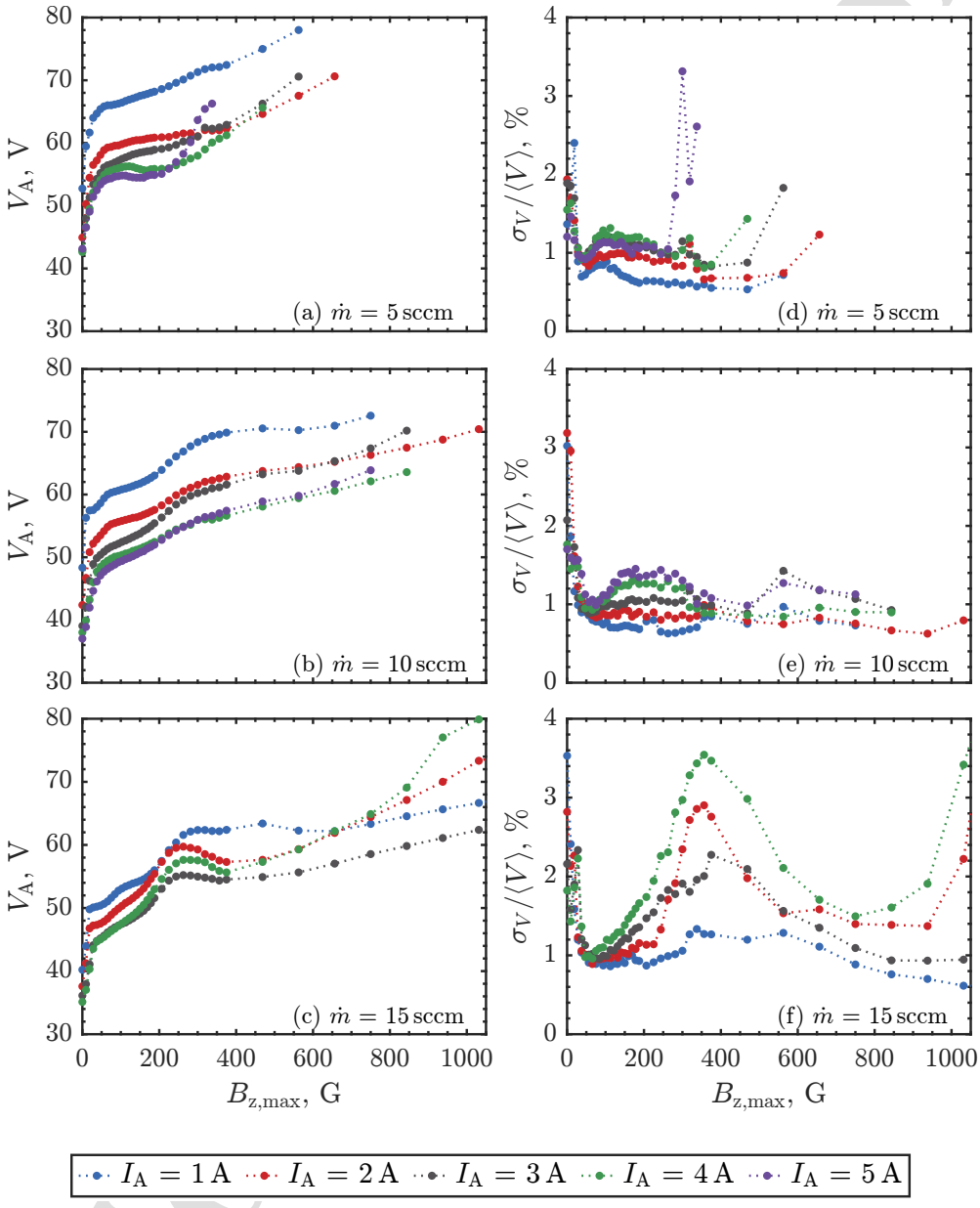


Figure 2: (a-c) Anode voltage V_A as a function of the maximum axial magnetic field $B_{z,max}$ for different mass flow rates $\dot{m}$ and anode currents I_A. (d-f) Relative standard deviation of V_A for the same cases.

relative to ground increases. When the effective impedance of the chamber-wall path becomes lower than that of the cathode–anode column, breakdown preferentially occurs along this alternate path, resulting in transient arcing accompanied by visible sputtering on nearby metallic surfaces. Arcing is observed to occur at lower magnetic field strengths for reduced mass flow rates, consistent with weaker collisional damping lowering the effective impedance of the chamber-wall path, and ultimately limits the maximum attainable B for stable operation in this configuration. It is emphasised that this limitation is specific to the present grounded configuration, in which the cathode, emitter, and chamber walls share a common electrical ground. In this arrangement the grounded chamber provides the alternate conduction path (R_{p2}) that competes with the cathode–anode column at high B; the arcing boundary is therefore a property of the test-stand grounding scheme rather than a fundamental limit of the thruster concept. Electrically isolating the discharge circuit from ground, allowing the cathode and emitter to float, would suppress this alternate path and is expected to extend the accessible field range substantially. This was not pursued here owing to the added complexity of integrating the grounded plasma diagnostics, but it represents the most direct route to higher stable operating fields in future implementations.

3.2. Plume Morphology and Selection of Diagnostic Cases

Magnetically induced changes in the visible plasma structure were assessed through plume imaging. Figure 4a shows the visible emission for increasing B at fixed $I_A = 3\,\mathrm{A}$ and $\dot{m} = 10\,\mathrm{sccm}$. At $B = 0$, the discharge is diffuse and only weakly collimated. As B increases, the plume contracts around the axis and develops a bright, elongated core extending further downstream. This behaviour is consistent with electron guiding along axial field lines, increased residence time, and enhanced local ionisation.

Mass flow rate also influences plume structure under magnetised conditions. At fixed I_A and B, lower $\dot{m}$ produces a brighter and more radially expanded plume, indicative of elevated electron temperatures in lower-collisionality regimes. Figure 4b illustrates this behaviour for $B_{z,\max} = 563\,\mathrm{G}$.

Five representative magnetic-field cases were selected based on the combined behaviour of the anode voltage, fluctuation levels, and plume structure for detailed

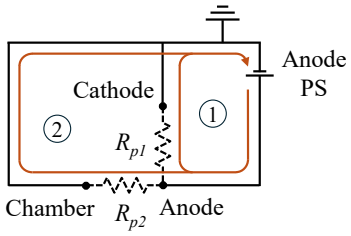
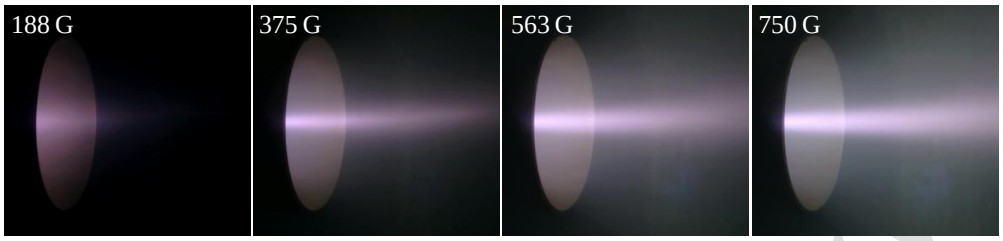
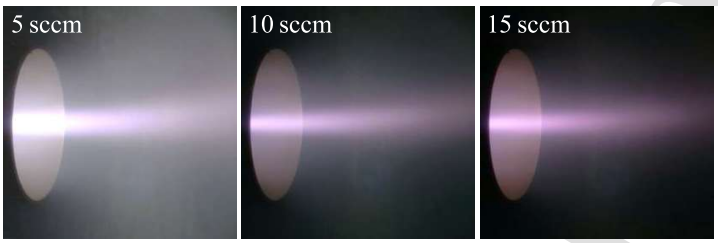


Figure 3: Simplified equivalent-circuit representation of the discharge illustrating the competing cathode–anode plasma column and chamber-wall conduction paths. The confined plasma column is represented by the effective impedance R_{p1}, while R_{p2} denotes the alternate conduction path to the grounded chamber. Loops (1) and (2) indicate the two possible current paths, with breakdown along the chamber-wall path corresponding to the onset of arcing at high magnetic field strengths.



(a) Images of the plasma plume for increasing B.



(b) Images of the plasma plume for increasing $\dot{m}$.

Figure 4: A series of images of the plasma plume for (top) increasing magnetic field strength at constant $I_\mathrm{A} = 3\,\mathrm{A}$ and $\dot{m} = 10\,\mathrm{sccm}$, and (bottom) increasing mass flow rate at constant $I_\mathrm{A} = 3\,\mathrm{A}$ and $B = 563\,\mathrm{G}$. The anode diameter is 150 mm.

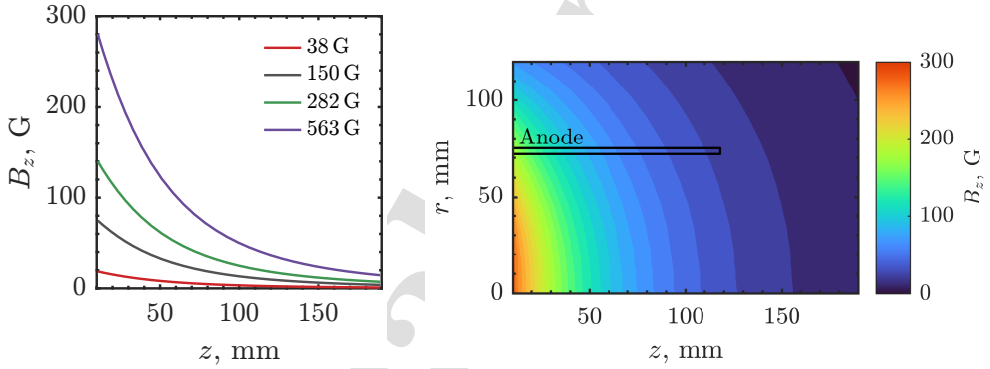


Figure 5: Magnetic field distribution for the applied field cases investigated. (a) On-axis field strength $B_z(z)$ over the measurement domain for each case. (b) Two-dimensional distribution of B_z across the measurement domain for the strongest case for which a full two-dimensional field map was acquired ($B_{z,\mathrm{max}} = 563\,\mathrm{G}$), from COMSOL Multiphysics simulations validated against on-axis measurements [14].

spatially resolved diagnostics with $B_{z,\mathrm{max}} = \{0,\ 38,\ 150,\ 282,\ 563\}\,\mathrm{G}$, all at $I_\mathrm{A} = 3\,\mathrm{A}$ and $\dot{m} = 10\,\mathrm{sccm}$. These cases span the relevant transitions from unmagnetised to strongly magnetised operation and capture the onset of confinement, the redistribution of plasma in the anode, and the formation of the bright on-axis plume. The corresponding on-axis magnetic field distributions for these cases, together with the two-dimensional field distribution for the strongest case for which full two-dimensional maps were acquired (563 G), are shown in Fig. 5.

Journal Pre-proof

4. Magnetic-Field Effects on the Plasma Plume

To determine how magnetic confinement modifies the spatial structure and energetics of the hollow cathode plume, the baseline operating point of $I_A = 3\,\mathrm{A}$ and $\dot{m} = 10\,\mathrm{sccm}$ is examined for the five representative cases in Sec. 3.2. Additional intermediate field cases are included to confirm the observed trends. The analysis combines electron-side diagnostics (EEPFs, n_e, $T_{e,\mathrm{eff}}$, V_p) with targeted ion measurements (IEDFs, beam parameters) to build a consistent picture of how axial magnetic fields reshape the plume and influence acceleration processes.

4.1. Measurement Constraints and Uncertainty

Preliminary Langmuir probe sweeps were acquired at each magnetic field strength to estimate the ion saturation current I_{sat} and floating potential V_f across the plume. These served to (i) identify symmetry planes, (ii) determine the maximum expected probe current, and (iii) establish a conservative probe-bias window for resolving the full I–V curve without excessive heating.

To prevent thermal damage to the 127μm probe tip, the maximum allowable current draw was limited to approximately 60 mA. As magnetic confinement strengthens and local density increases, this constraint imposes a change in the minimum accessible axial position $z_{\min}$. For the five principal magnetic field cases, empirical limits of $z_{\min} = 1\,\mathrm{cm}$ (0 and 38 G), 2 cm (150 G), 5 cm (282 G), and 10 cm (563 G) were established from early test sweeps. This constraint is fundamental rather than procedural: at $B_{z,\max} = 563\,\mathrm{G}$, the electron saturation current at $z < 10\,\mathrm{cm}$ exceeds the $\approx 60\,\mathrm{mA}$ thermal limit before the full I–V sweep can be completed, rendering EEPF extraction unreliable regardless of sweep parameters. Increasing the probe radius to permit larger current draw would violate the condition $r_p \ll r_{L,e}$ required for valid EEPF extraction in a magnetised plasma [16], and was therefore not pursued. Access to the near-cathode region at high B remains unmeasured in the present work. Non-invasive diagnostics such as laser-induced fluorescence or Thomson scattering are identified as the appropriate approach for future investigation of this region.

As established in Sec. 2.3, $r_p \ll r_{L,e}$ is satisfied throughout; the same holds for ions, with $r_{L,i} \sim 30\,\mathrm{mm}$ for the strongest fields considered, so both electrons and ions can be treated as effectively unmagnetised on the scale of the probe, avoiding magnetically induced probe collection artefacts [16]. This conclusion is conservative for the ion measurements discussed in Sec. 4.6: the on-axis field decays substantially downstream of the anode exit (Fig. 5a), so at the RPA measurement locations ($z = 15$–$27\,\mathrm{cm}$) the local field is a small fraction of $B_{z,\max}$, and the ion gyroradius there exceeds the $r_{L,i} \sim 30\,\mathrm{mm}$ estimate above. The RPA-derived IEDFs and beam parameters therefore reflect a genuine electrostatic acceleration signature rather than a magnetically modified collection response. The same decay indicates that plasma potential measurements in this downstream region are not confounded by field-dependent probe response, consistent with the $\pm 2\,\mathrm{V}$ agreement between the Langmuir and emissive probes reported above. This also clarifies the limited constraining effect of the applied field on beam divergence evident in Fig. 4: since ions are effectively unmagnetised over most of the plume, the collimation observed in the density and potential maps (Secs. 4.3 and 4.4) is attributable primarily to

Journal Pre-proof

electron-guided transport and electrostatic focusing rather than direct magnetic confinement of the ions themselves.

Signal fluctuations become more pronounced with increasing B, particularly in the floating potential and the low-energy region of the EEPFs. This behaviour is consistent with magnetically enhanced plasma oscillations and modifications of the sheath. As noted in Sec. 2.3, the discharge was operated in a lightly loaded regime not typically associated with plume-mode onset; oscillation-induced distortion is therefore expected to be limited, though it cannot be excluded in individual measurements.

In a localised region at low z and large r for the 38 G case, the low-energy gap in the EEPF becomes anomalously large and noisy, reminiscent of the distortion produced by oscillating plasma potential [19, 20]. Because the Langmuir probe I–V characteristic is nonlinear, time-averaging over plasma-potential oscillations produces $\langle I(V - V_p(t))\rangle \neq I(V - \langle V_p\rangle)$: the distortion is largest near V_p where the I–V slope is steepest, and is amplified by the second derivative required for EEPF extraction [19]. The anomaly is spatially concentrated at low z and high r, the region of steepest radial density gradient at this intermediate field strength, consistent with gradient-driven oscillatory modes expected at the transitional magnetisation of 38 G. This attribution is supported by high-bandwidth floating potential measurements at a reference on-axis location: the peak-to-peak variation was approximately 0.34 V in the absence of an applied field, rising to approximately 2 V at 38 G before decreasing again at higher field strengths, consistent with a mode localised to the transitional regime rather than a persistent instability. Time-resolved probe measurements would be required to characterise the oscillation spectrum fully. At these locations, the relative uncertainty in the EEPF-derived quantities exceeds 100 %, and the affected data are excluded. Plasma potential values from the emissive probe and densities derived from the electron saturation branch (OML analysis) are used instead and agree well with EEPF-based densities elsewhere.

The uncertainty in the EEPF-derived parameters was estimated by combining three contributions in quadrature: (i) the fit uncertainty associated with the Druyvesteyn-type correction used to account for the low-energy gap in the EEPF, (ii) the sensitivity to the low-energy gap correction itself, and (iii) the statistical scatter across repeated measurements. Across the full dataset, the resulting relative uncertainties range from approximately 7–14 % for $T_{\mathrm{e,eff}}$ and 4–9 % for n_{e}. For clarity, the upper bounds of these ranges are adopted here as representative uncertainties, yielding ± 14 % for $T_{\mathrm{e,eff}}$ and ± 9 % for n_{e}. The uncertainty in plasma potential is estimated at ± 2 V based on the average deviation between emissive and Langmuir probe measurements. For clarity, error bars, or a representative error bar, are shown on the axial and parametric trend figures throughout Secs. 4.3–4.6; the same relative uncertainties stated above apply equally to the radial profiles presented elsewhere, where error bars are omitted to preserve legibility given the number of overlapping series.

4.2. Evolution of the Electron Energy Probability Function

The axial evolution of the EEPF along the central axis for a representative intermediate field ($B_{z,\max} = 282$ G) is shown in Fig. 6. A well-defined low-energy bulk population is maintained over the entire measured axial range, from just downstream

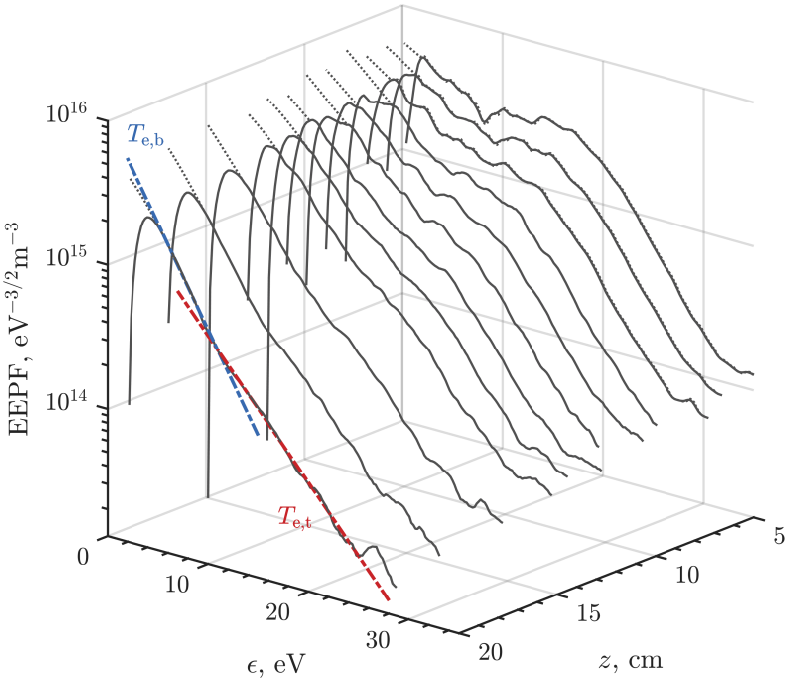


Figure 6: Axial evolution of the electron energy probability function (EEPF) along the central axis at $B_{z,\max} = 282\,\mathrm{G}$, $I_\mathrm{A} = 3\,\mathrm{A}$ and $\dot{m} = 10\,\mathrm{sccm}$. Profiles are shown at discrete axial distances from the cathode. Dotted lines represent the applied low-energy gap correction. Red and blue dashed lines indicate example linear fits at $z = 19\,\mathrm{cm}$ to the high-energy tail and bulk used to extract characteristic temperatures $T_{e,\mathrm{t}}$ and $T_{e,\mathrm{b}}$ respectively.

of the cathode orifice to the furthest location at $z = 19\,\mathrm{cm}$. Superimposed on this, a distinct high-energy tail persists at all positions. Example linear fits to the bulk and tail at $z = 19\,\mathrm{cm}$ illustrate how two characteristic temperatures, $T_{\mathrm{e,b}}$ and $T_{\mathrm{e,t}}$, can be extracted. Closer to the cathode, a pronounced secondary hump is visible on the high-energy side of the EEPF, corresponding to a beam-like electron population. As the plume expands downstream, this feature gradually merges into the broader tail.

The continued presence of a high-energy tail, even at the furthest downstream location, demonstrates incomplete thermalisation of the electron population under confinement. At the same time, the sustained bulk population suggests that local losses are reduced. To assess whether local ionisation contributes to maintaining the bulk, the ionisation mean free path was estimated using the measured EEDF at $z = 50\,\mathrm{mm}$. The number density of electrons with $\varepsilon > 15.76\,\mathrm{eV}$ is approx. $9 \times 10^{16}\,\mathrm{m}^{-3}$, and the effective ionisation cross-section is $\sim 2 \times 10^{-20}\,\mathrm{m}^2$. Combined with an estimated neutral density based on the background pressure ($\sim 0.5\,\mathrm{mTorr}$) and $T_\mathrm{g} \approx 500\,\mathrm{K}$, this yields a mean free path of tens of metres, far exceeding the plume length. No significant depletion is observed in the EEPF above the ionisation threshold, further confirming that downstream ionisation is negligible. Consequently, the measured distributions are best interpreted as magnetically confined, weakly thermalised EEPFs with reduced losses and a persistent energetic electron tail.

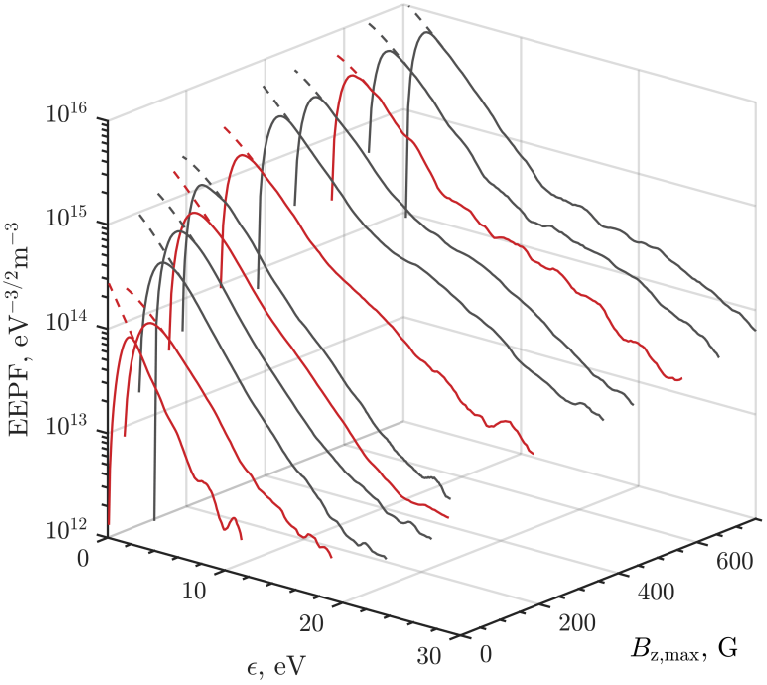


Figure 7: Evolution of the measured EEPFs at the furthest point in the plume for increasing applied magnetic field strengths. The curves highlighted in red are those at the chosen conditions $B_{z,\max}$ = (A) 0, (B) 38, (C) 150, (D) 282 and (E) 563 G. Dashed lines represent the low-energy gap correction applied.

Figure 7 shows the EEPF measured at the furthest downstream location ($z = 19$ cm) for increasing magnetic field strength. At $B = 0$ G, the EEPF is approximately single-Maxwellian with a relatively low effective temperature, consistent with a rarefied distribution subject to strong axial and radial losses. The apparent high-energy tail in the 0 G curve lies at the absolute noise floor of the analogue second-derivative signal, reached at this lowest-density condition, and reflects measurement noise rather than a physical high-energy electron population. As B increases, the distribution broadens and the high-energy tail becomes progressively more populated. A distinct transition occurs around $B_{z,\max} \approx 250$ G, beyond which the tail becomes dominant and the effective electron temperature rises sharply.

The area under the EEPF, and hence the electron density, also increases markedly with magnetic field strength at this location, before gradually plateauing beyond $B_{z,\max} \gtrsim 400$ G. In the absence of downstream ionisation, this increase must stem from changes nearer the cathode: enhanced confinement increases electron residence times, supporting more upstream ionisation, while suppressing radial losses. The subsequent saturation suggests that once the existing electron population is efficiently confined, further increases in B yield diminishing returns in local density enhancement.

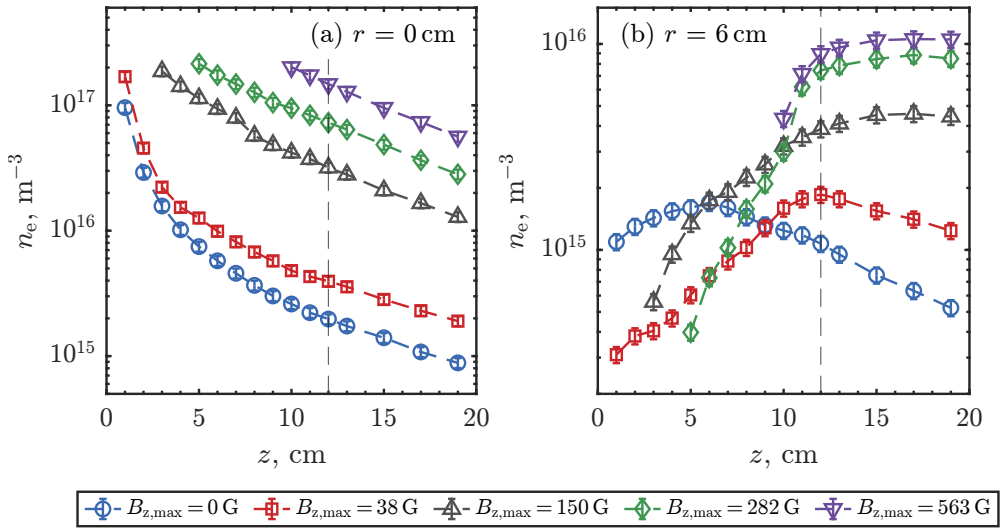


Figure 8: Axial profiles of the electron density for all applied field strengths: (a) along the central axis ($r = 0$ cm), (b) along the most radial profile near the anode wall ($r = 6$ cm). The vertical dashed lines indicate the anode exit plane.

4.3. Electron Density and Radial Confinement

Two-dimensional maps of the time-averaged electron number density $n_e(r, z)$ for increasing $B_{z,max}$ are presented in Fig. 9. With no applied field, the plume is diffuse and expands rapidly both axially and radially. As B increases, the plume contracts into a denser, more collimated structure. The density contours progressively align with the magnetic field lines, reflecting the increasing dominance of field-guided transport.

The suppression of radial expansion is particularly evident at higher values of B, where the dense core remains confined close to the axis over an extended axial range. This behaviour is consistent with reduced cross-field mobility due to electron gyromotion and enhanced residence times in the high-B region.

Axial profiles of n_e along the centreline are shown in Fig. 8(a). The electron density at the anode exit and further downstream increases substantially with magnetic field strength, while the downstream decay rate beyond the anode remains similar across cases. This suggests that radial confinement and upstream ionisation are the main drivers of the density increase, whereas axial transport is only weakly affected.

Figure 10 presents the non-linear dependence of n_e on magnetic field strength. At low fields, n_e increases steeply with increasing B, reflecting gains from improved confinement. The density approaches a plateau above approximately $B_{z,max} \approx 400$ – 500 G. Across the full range $B_{z,max} = 0$ – 750 G, the on-axis density at $z = 19$ cm increases by nearly two orders of magnitude, from 8.8×10^{14} to 7.0×10^{16} m^{-3}.

Radial profiles at fixed axial positions (Fig. 11) highlight the growing impact of magnetic confinement on plume width. As B increases, the density peaks become sharper and the radial extent of the plume narrows. At $B_{z,max} = 563$ G, the plume remains tightly confined even at $z = 19$ cm.

These results demonstrate that axial magnetic fields can strongly collimate

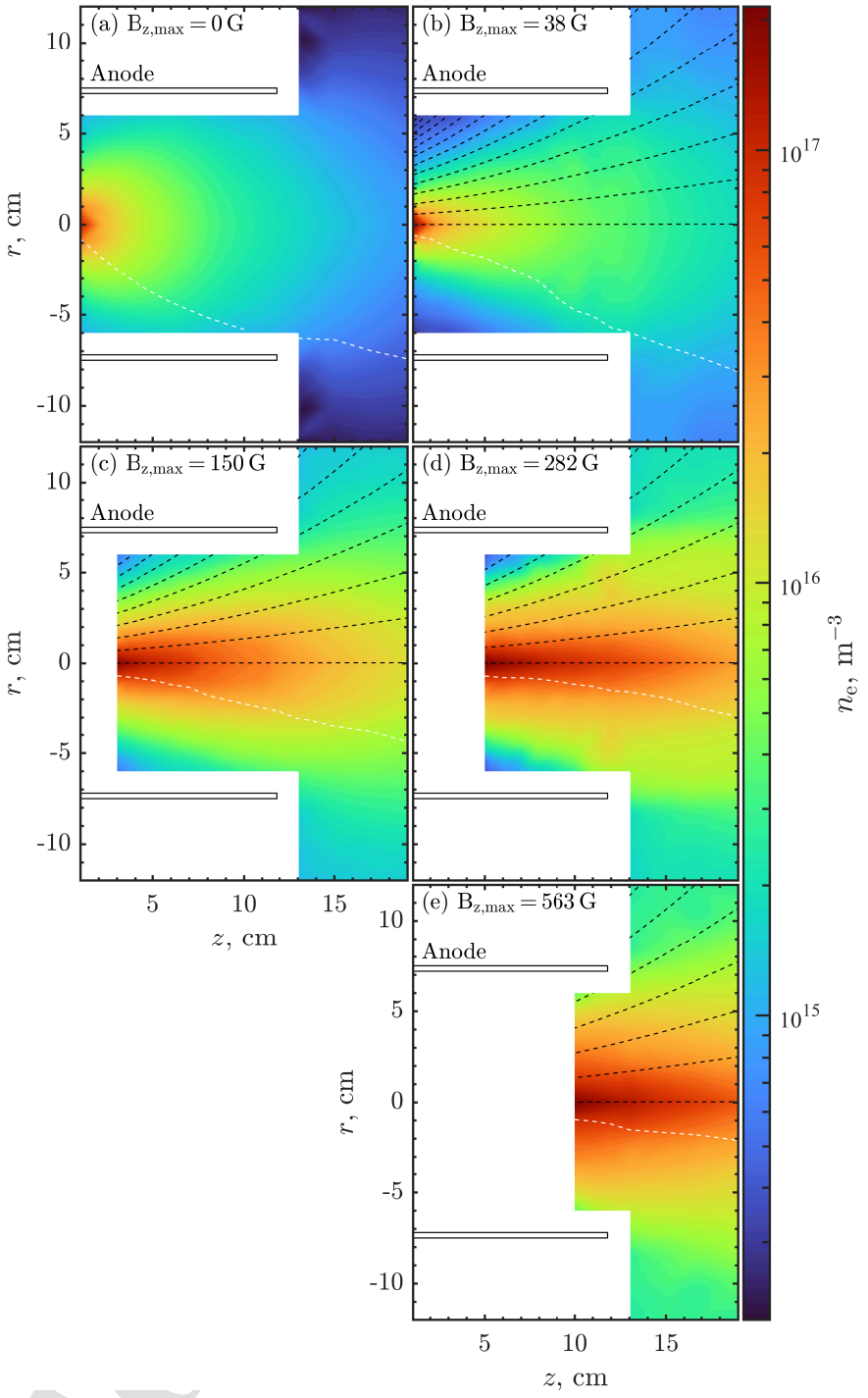


Figure 9: Two-dimensional (r–z) spatial contours of the time-averaged electron density n_e for increasing axial magnetic field strength. Magnetic field lines are shown for one half of the domain. Data are mirrored about the axis.

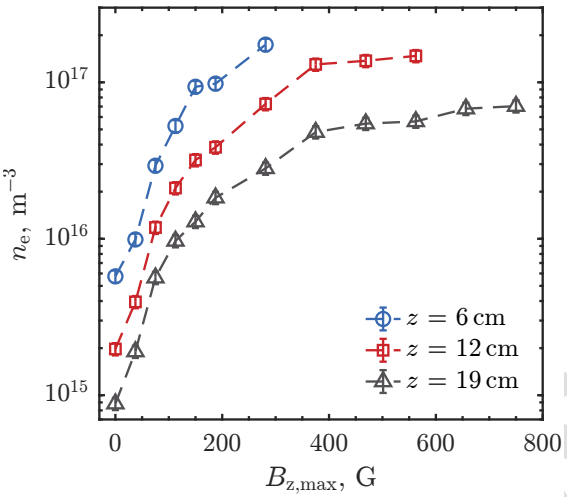


Figure 10: Electron density n_e measured on the central axis ($r = 0$ cm) at three axial positions as a function of the maximum applied axial magnetic field strength $B_{z,max}$.

a hollow cathode plume, increasing the on-axis electron density by nearly two orders of magnitude while suppressing radial losses. The observed redistribution of electrons along the anode length also provides an explanation for the non-linear $V_A(B)$ behaviour; as confinement shifts the bulk plasma downstream and away from portions of the anode, the effective current path length and resistance change, producing the characteristic slope changes in the anode voltage curve. This density–resistance coupling is supported by the observed inverse relationship between the integrated electron density near the anode wall and the anode voltage: conditions with a higher near-anode electron population consistently draw the discharge current at a lower

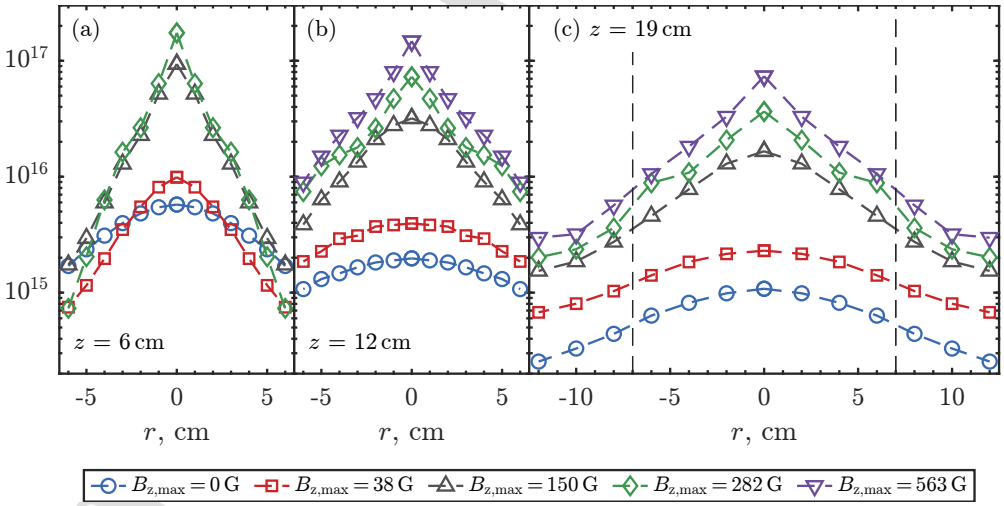


Figure 11: Radial profiles of electron density n_e at three axial positions: (a) $z = 6$ cm, (b) $z = 12$ cm, and (c) $z = 19$ cm, for increasing maximum applied axial magnetic field strengths $B_{z,max}$.

V_A, consistent with a reduced effective discharge resistance. This framework offers a hypothesis for the non-monotonic $V_A(B)$ behaviour observed at $\dot{m} = 15$ sccm, where a local maximum appears near $B \approx 250$ G (Fig. 2). At this highest flow rate the neutral density, and hence collisionality, is greatest, giving the shortest ionisation mean free path. Below ∼250 G, increasing confinement shifts the ionisation zone and bulk plasma downstream, depleting the near-anode density and raising V_A. Near 250 G, the elevated collisionality at 15 sccm may allow the ionisation zone to partially re-anchor toward the inner anode surface, transiently increasing the local density and lowering the effective resistance, which would produce the observed dip in V_A. At still higher fields, strong magnetic confinement again drives the plasma downstream past the anode exit and the voltage resumes its rise. At lower flow rates (5 and 10 sccm) the longer ionisation mean free path weakens or removes this intermediate re-anchoring, shifting the balance to higher fields or beyond the accessed range. This account remains a hypothesis and should not be regarded as an established mechanism. The spatially resolved density maps presented here were acquired only at 10 sccm, and the proposed re-anchoring of the ionisation zone at 15 sccm has not been observed directly. Spatially resolved density measurements at 15 sccm across the range $B_{z,\max} \approx 150$–400 G are required to verify it, ideally complemented by segmented-anode or time-resolved measurements of the current attachment.

4.4. Plasma Potential Structure and Electrostatic Nozzle Formation

Two-dimensional maps of the time-averaged plasma potential $V_p(r, z)$ are shown in Fig. 13 for the same set of magnetic field strengths. With no applied field, the potential exhibits a weak axial gradient downstream of the anode and near-radial symmetry. As B is increased, the overall magnitude of V_p rises and the axial gradient progressively steepens, while the equipotential contours develop a pronounced nozzle-like shape characterised by curved radial profiles.

Along the plume axis (Fig. 12), the plasma potential becomes more positive

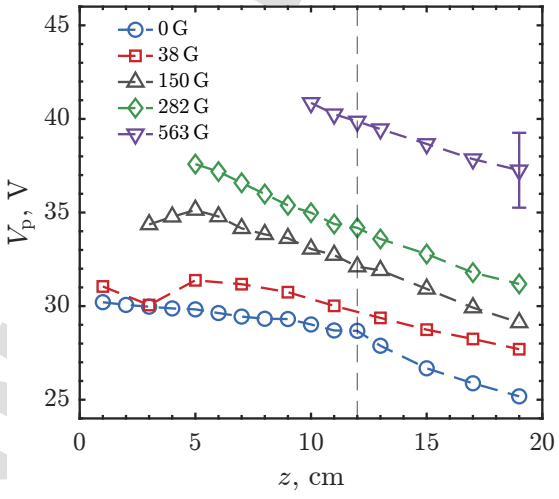


Figure 12: Axial plasma potential profiles $V_p(z)$ along the central axis for increasing magnetic field strength. A representative error bar is shown; see Sec. 4.1 for the associated uncertainty.

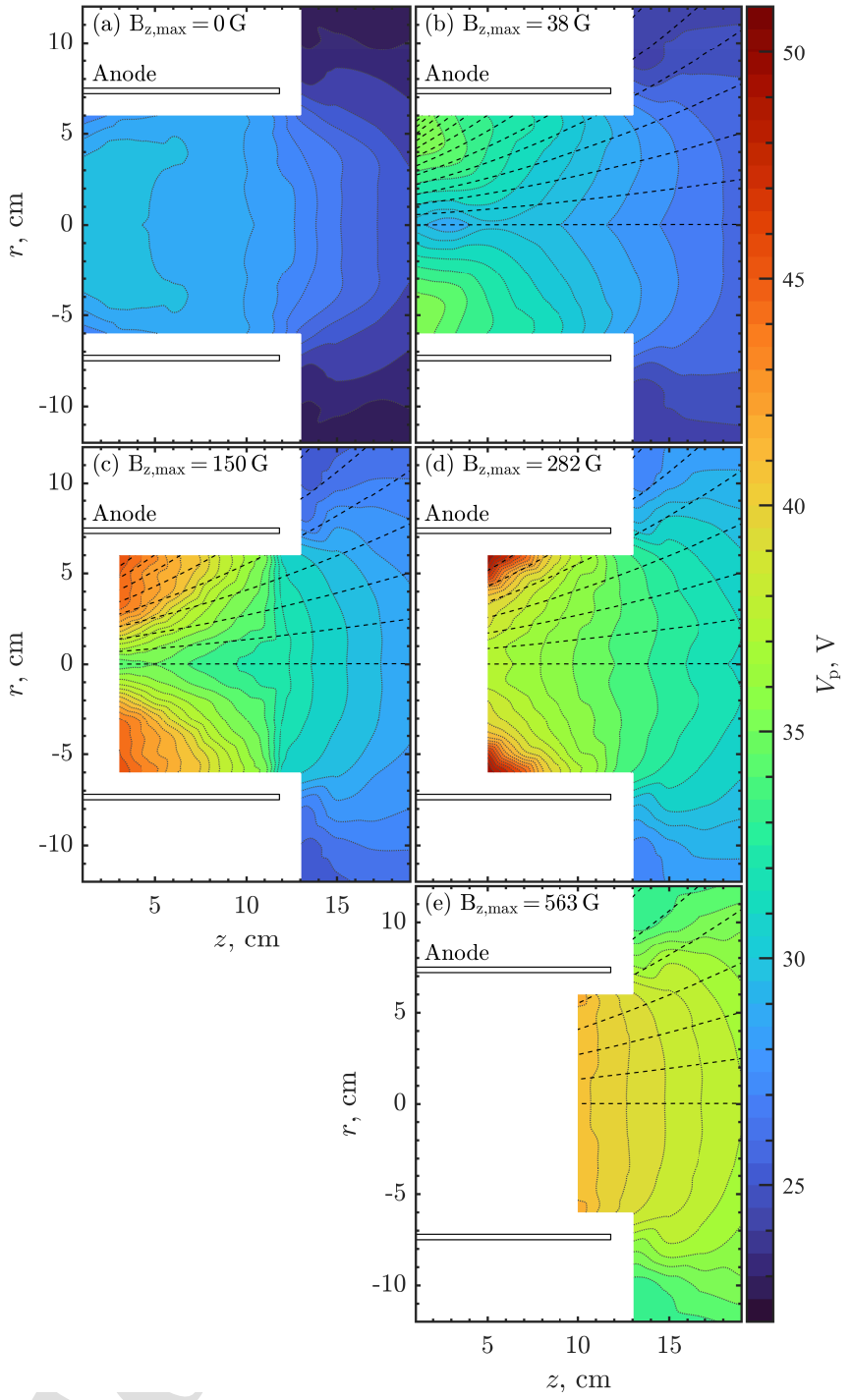


Figure 13: Measured two-dimensional (r–z) spatial profiles of the time-averaged plasma potential V_p for increasing axial magnetic field strengths. Magnetic field lines are shown for one half of the domain. Data are mirrored about the axis.

Journal Pre-proof

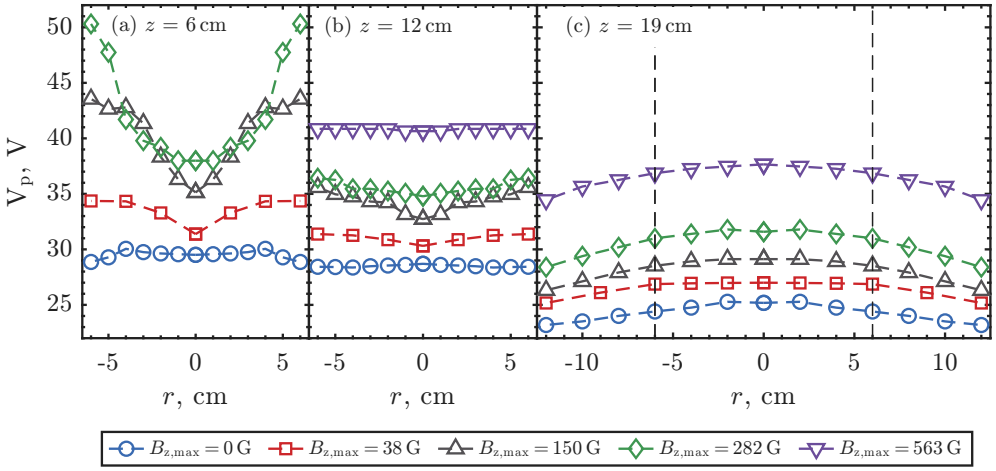


Figure 14: Radial plasma potential profiles $V_p(r)$ at (a) $z = 6$ cm, (b) 12 cm, and (c) 19 cm for increasing magnetic field strengths.

overall with increasing field strength and develops a stronger axial drop downstream of the anode. For intermediate fields (e.g. 38 and 150 G), a local dip followed by a rise in V_p appears near the cathode, forming a negative potential hill. This structure would act to impede low-energy ions near the cathode orifice and is consistent with the strongly fluctuating region in which Langmuir probe measurements were compromised. Similar potential dips have been reported in other hollow cathode configurations and linked to dense near-cathode plasma regions [12].

Radial profiles of V_p at fixed z (Fig. 14) reveal the emergence of a concave radial potential well as B increases. At $z = 6$ cm, the on-axis potential minimum deepens with field strength, generating radially inward electric fields that focus ions toward the axis. Further downstream, the radial gradient decreases but the minimum remains discernible, indicating sustained electrostatic focusing over the measurement domain. The single-point E_r estimate given below (Sec. 4.5) is illustrative of conditions throughout the steep-gradient zone visible in the V_p contours of Fig. 13, which extends over a broad conical region coinciding with the outer boundary of the electrostatic nozzle rather than being confined to a single location.

These features support the interpretation that the applied field induces an electrostatic nozzle structure; the combination of steep axial and inward radial electric fields leads to both axial acceleration and radial compression of ions, while guiding electrons toward the increasingly positive anode under constrained cross-field transport.

4.5. Electron Temperature and High-Energy Structures

The effective electron temperature maps shown in Fig. 15 share several of the features of density and potential results. With increasing B, a narrow, high-temperature axial core forms that becomes more pronounced and extends further downstream. This hot core coincides with the high-density region in n_e and reflects the persistence of a high-energy tail population under confinement, as discussed in Sec. 4.2.

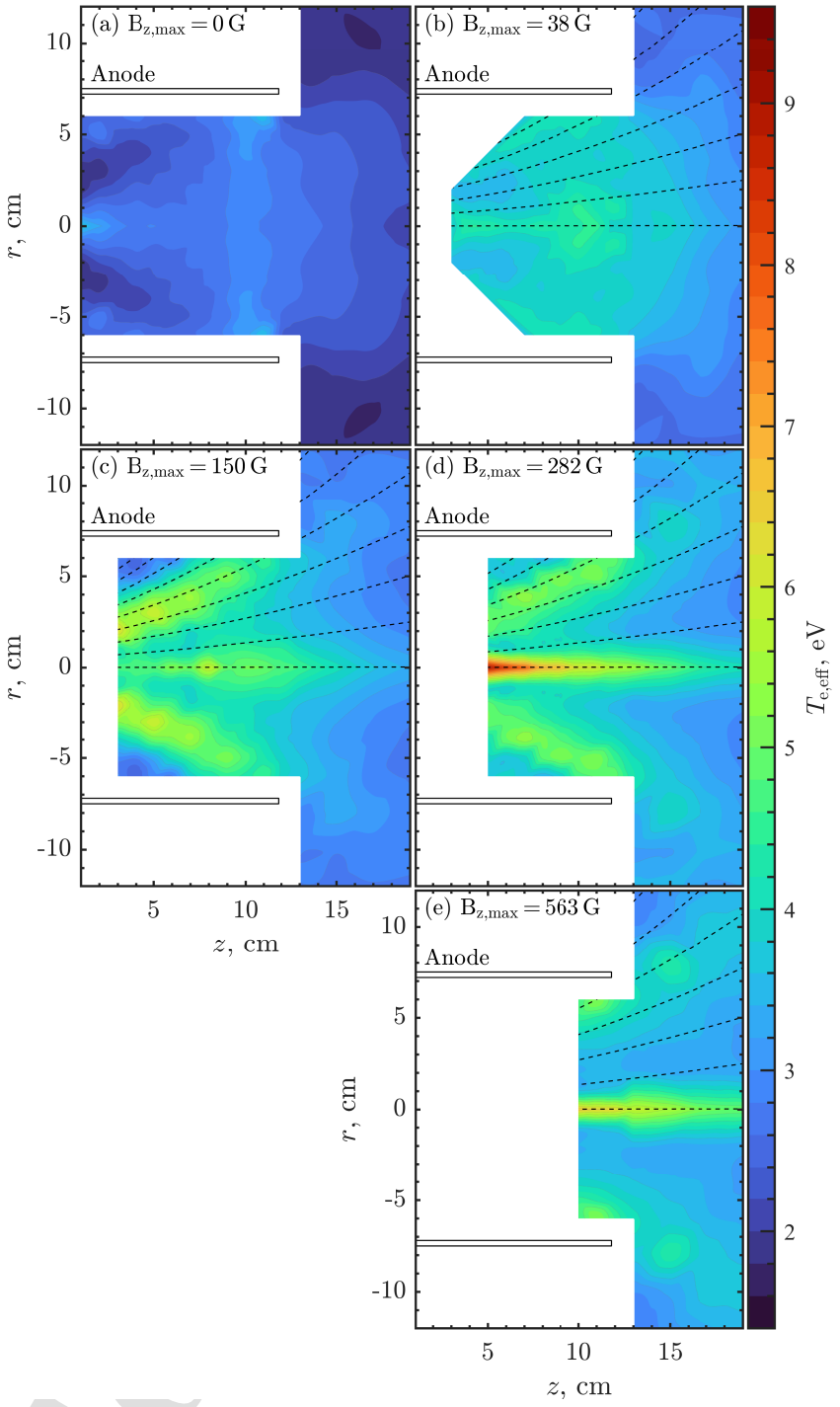


Figure 15: Two-dimensional (r–z) spatial profiles of the time-averaged electron temperature $T_{e,eff}$ for increasing axial magnetic field strengths. Magnetic field lines are shown for one half of the domain. Data are mirrored about the axis.

Journal Pre-proof

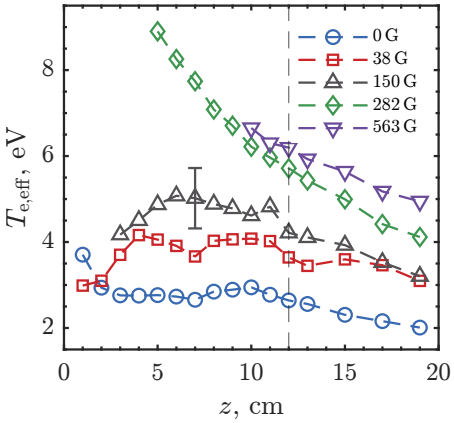


Figure 16: Axial profiles of the effective electron temperature $T_{e,eff}$ along the centreline of the plume for increasing magnetic field strengths. The vertical dashed line marks the anode exit location. A representative error bar is shown; see Sec. 4.1 for the associated uncertainty.

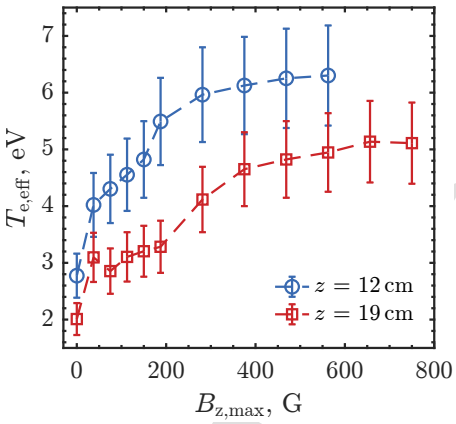


Figure 17: Effective electron temperature $T_{e,eff}$ measured on the central axis ($r = 0$ cm) at two axial positions as a function of the maximum applied magnetic field strength $B_{z,max}$.

Centreline profiles of $T_{e,eff}$ (Fig. 16) indicate that, for low to moderate fields, the temperature initially increases with distance before gradually decaying, similar to the non-magnetised case but at higher absolute values. For example, at $z \approx 6$ cm the effective temperature rises from approximately 3 eV at $B = 0$ to about 6–7 eV at $B_{z,max} = 282$ G. At stronger fields, $T_{e,eff}$ increases further and the axial decay decreases, reaching up to ~ 9 eV near the anode exit and remaining elevated downstream. Parametric data in Fig. 17 show that, like n_e, $T_{e,eff}$ eventually plateaus with B, suggesting saturation of the confinement-induced heating.

At $B_{z,max} \gtrsim 150$ G, a secondary region of elevated electron temperature appears off-axis, forming a conical structure along the outer field lines that do not intersect with the anode. This region is not associated with a corresponding density enhancement and the local EEPFs do not exhibit sufficient high-energy content to support significant ionisation. Two mechanisms are considered to explain this phenomenon.

First, this region may be populated by cathode-emitted electrons that are deflected off-axis early in the discharge or emitted with a radial component of velocity, becoming trapped along non-intersecting field lines in relatively collisionless regions. These electrons can retain much of their initial kinetic energy as they move downstream, leading to locally elevated effective temperatures without a corresponding increase in density.

Second, comparison with the plasma potential maps indicates that the conical high-T_e region approximately aligns with steep potential gradients. In such regions, strong radial electric fields combined with axial B give rise to azimuthal $\mathbf{E} \times \mathbf{B}$ drift. For example in the $B_{z,max} = 282$ G case, the steepest local gradients in the measured potential near the anode ($r \approx 5$–6 cm, $z \approx 5$ cm) reach E_r of order 2000 V/m, though gradients across the broader steep-gradient zone are typically several hundred V/m. Taking an upper-bound representative $E_r \sim 10^3$ V/m with $B_z \approx 50$ G, the azimuthal

Journal Pre-proof

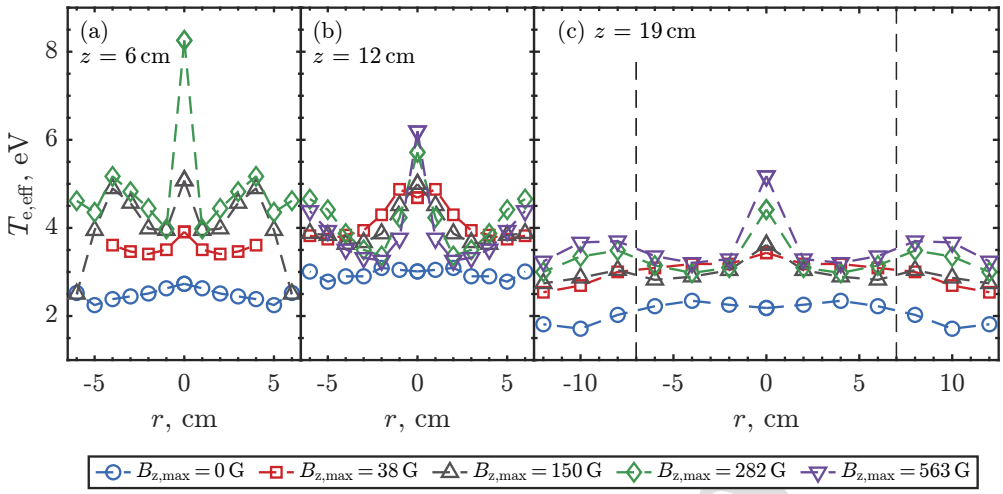


Figure 18: Radial effective electron temperature profiles $T_{\mathrm{e,eff}}$ at (a) $z = 6\,\mathrm{cm}$, (b) 12 cm, and (c) 19 cm for increasing magnetic field strengths. The vertical dashed lines mark the radial anode extent.

drift velocity is

$$v_\eta = \frac{E_r}{B_z} \sim 2 \times 10^5\,\mathrm{m/s}, \tag{1}$$

of order 20 % of the thermal velocity of 3 eV electrons. Such drifts can drive significant azimuthal currents and associated Joule heating, leading to locally elevated electron temperatures that are then advected downstream along the field lines.

Of the two proposed mechanisms, the spatial structure of the feature more closely favours the $\mathbf{E} \times \mathbf{B}$ heating picture. At intermediate fields ($B_{z,\mathrm{max}} = 150$ and 282 G), where both the off-axis structure and the near-anode potential field are well resolved, the off-axis high-T_e region forms a conical structure at high r and low-to-moderate z. This region coincides with the steep radial gradient in the plasma potential, where V_p falls from its peak near the anode toward the axis over a short radial distance (compare Figs. 15 and 13). Such co-location of elevated T_e with the region of strongest radial potential gradient is a natural consequence of localised Joule heating by the azimuthal $\mathbf{E} \times \mathbf{B}$ drift at the nozzle boundary, whereas the trapped-electron mechanism provides no reason for the hot region to coincide specifically with the steep-gradient zone. This interpretation is consistent with reports of similar high-T_e ridgelines aligned with steep potential gradients in other magnetised hollow cathode and applied-field MPD configurations, often linked to swirl acceleration and radial-to-axial momentum conversion [21]. The feature emerges only at $B_{z,\mathrm{max}} \gtrsim 150\,\mathrm{G}$, consistent with the onset of a well-developed nozzle potential structure at these fields. Both mechanisms may contribute, and definitive resolution would require direct measurement of the azimuthal current density or non-invasive spectroscopic diagnostics; this is identified as future work.

Radial profiles of $T_{\mathrm{e,eff}}$ (Fig. 18) highlight both the sharp central peak and the development of the off-axis hot region. The central temperature maximum strengthens with B and remains confined to small radii, while the off-axis peak moves

Journal Pre-proof

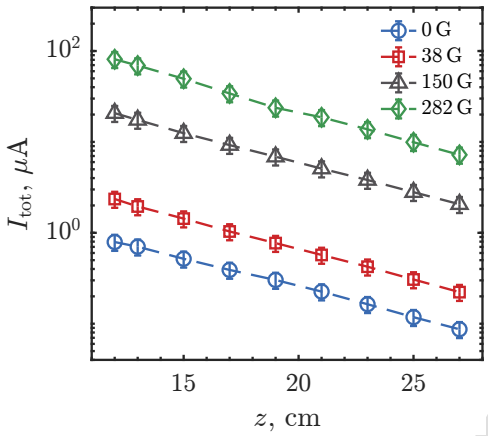


Figure 19: Axial profiles of the total ion current I_0 measured with the RPA along the plume central axis for increasing magnetic field strength $B_{z,\max}$.

outward along the diverging outer field lines and remains visible even at $z = 19\,\mathrm{cm}$.

4.6. Ion Beam Characteristics

To assess whether the electron-side changes translate into enhanced ion acceleration, a set of retarding potential analyser measurements was performed along the plume centreline between $z = 15$ and 27 cm for selected field strengths ($B_{z,\max} = 0$, 38, 150 and 282 G). Although limited in spatial coverage due to probe size and fragility, these measurements provide useful insight into on-axis ion beam formation.

The total collected ion current I_{tot} at 0 V discriminator voltage is shown in Fig. 19. The uncertainty in I_{tot} was assessed by comparing the directly measured collector current at $V_{\mathrm{D}} = 0$ against the value reconstructed by integrating the corresponding IEDF; across the dataset the two agree to within a representative $\sim$20 %. With increasing magnetic field, the measured ion current rises at all axial positions, consistent with the higher on-axis densities and improved radial confinement inferred from the electron measurements. The axial decay rate of I_{tot} is similar across cases, suggesting that background neutral collisions dominate the downstream attenuation of the ion beam.

Example IEDFs for the unmagnetised case are shown in Fig. 20. Near the anode exit, the distribution is dominated by a peak associated with thermal ions at the local plasma potential. As z increases, the main peak shifts to lower energy as V_{p} decays, while a higher-energy shoulder evolves into a distinct secondary peak, indicating the emergence of an axial ion beam.

The influence of magnetic confinement on the IEDF at the furthest downstream location is shown in Fig. 21. The distributions exhibit a substantial increase in overall energy content and amplitude with increasing B, in agreement with the rise in I_{tot}. The high-energy portion of the IEDF becomes increasingly populated, although the secondary peak becomes less distinct as the beam and bulk overlap more strongly at higher fields. It should be noted that downstream single-peaking of the IEDF is not the expected outcome in this plume. The argon charge-exchange mean free path is comparable to the measurement path, as discussed below in the context of the

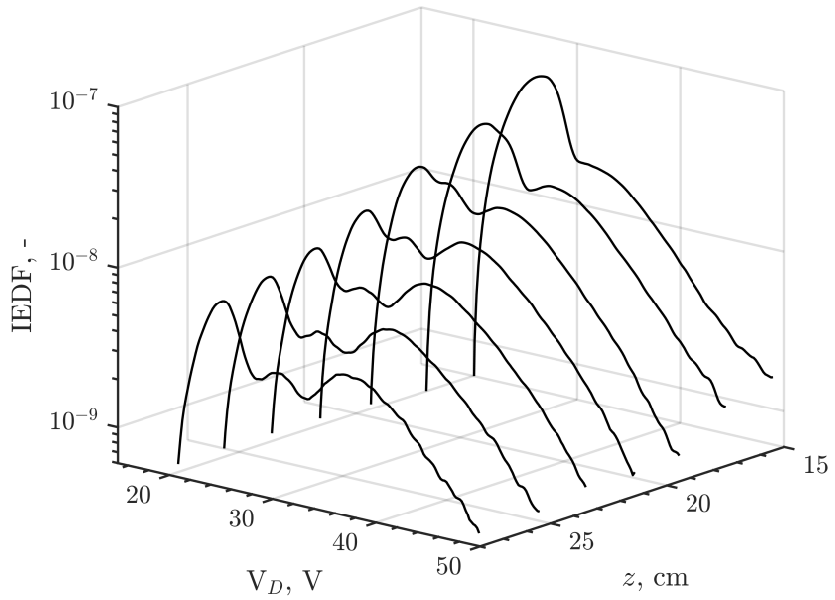


Figure 20: Axial evolution of the IEDF along the central axis $r = 0\,\mathrm{cm}$ for the baseline condition $I_\mathrm{A} = 3\,\mathrm{A}$ and $\dot{m} = 10\,\mathrm{sccm}$ with $B_{\mathrm{z,max}} = 0\,\mathrm{G}$.

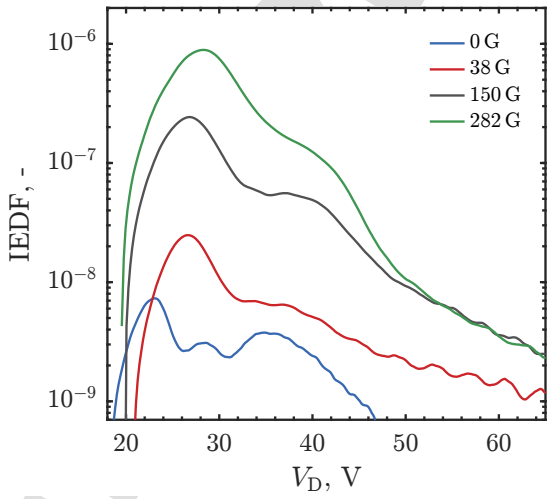


Figure 21: Measured IEDFs for increasing magnetic field strengths $B_{z,\mathrm{max}}$ at the furthest axial measurement point, $z = 27\,\mathrm{cm}$.

ion beam velocity, so some attrition of the directed population by charge exchange is expected; however, the RPA is a directional instrument that measures the axial-energy projection of ions entering its acceptance cone, and a resolvable beam peak requires only that a ballistic, least-scattered subset of the directed population survive to reach the analyser, not that the population as a whole propagate collisionlessly.

Journal Pre-proof

This is consistent with the persistence of a resolvable secondary peak at the furthest measurement station ($z = 27\,\mathrm{cm}$) across all field cases, alongside its decreasing amplitude relative to the bulk. At higher field strengths the secondary peak becomes less distinct not necessarily due to thermalisation, but because the rising beam-to-background current ratio increases the overlap between the two populations in the deconvolution, even as they remain energetically distinct. Apparent single-peaking at greater downstream distances could additionally arise from geometric acceptance-angle mixing as the diverging plume populates the RPA acceptance cone with ions of increasingly varied source angle, or from flattening of the source potential structure; these are instrumental and source effects rather than thermalisation, and are not excluded by the present measurements. The use of the RPA is therefore appropriate in the present operating regime, where the relatively low discharge current (3 A) and applied magnetic field ($B_{z,\max} \leq 282$ G) are insufficient to drive significant azimuthal swirl at the centreline. Furthermore, the measured plasma-potential distributions exhibit smooth, monotonic axial gradients without evidence of helical transport, supporting the assumption that the ion motion remains predominantly axial over the measurement region. Because the RPA measures a directional energy projection, the IEDF peaks are interpreted as a streaming/birth-potential signature rather than a thermodynamic spectrum, and the Gaussian decomposition is treated as a diagnostic decomposition of that signature rather than a claim about equilibrium populations. At substantially higher discharge currents or magnetic field strengths, where non-axial ion motion may become significant, an energy-angle-resolved diagnostic would be required to fully characterise the ion velocity distribution.

Gaussian deconvolution of the IEDFs enables extraction of the local plasma and beam potentials (V_p and V_B). These are plotted in Fig. 22, alongside independent V_p measurements from Langmuir and emissive probes. The plasma potentials from all diagnostics show consistent trends and continue the downstream decay observed within the anode region. The beam potential remains significantly higher than the local plasma potential, confirming the presence of an accelerated ion population.

From the potential difference $V_\mathrm{B} - V_\mathrm{p}$, the beam velocity v_b is estimated (with uncertainties of order $\pm 900\,\mathrm{m/s}$). The resulting profiles (Fig. 23) indicate beam speeds of $\sim$6–7 km/s for all fields investigated, with only minor variations within the uncertainty bands. The approximate constancy of v_b with increasing B warrants explanation. Inspection of Fig. 22 shows that both V_B and V_p rise with increasing field strength: as magnetic confinement strengthens, the entire electrostatic nozzle potential structure shifts upward globally, but the accelerating potential drop $\Delta V = V_\mathrm{B} - V_\mathrm{p}$ at the measurement location remains approximately constant. The primary effect of stronger confinement is therefore to increase the number of ions entrained in the beam, reflected in the strong rise of I_B, rather than to deepen the accelerating potential well. This is consistent with the saturation of electron density and temperature at high B: once confinement is effective, further field increases do not substantially alter the energy budget per ion. An additional floor on measurable beam energy spread is imposed by charge-exchange collisions at background pressures of 0.5–0.8 mTorr over measurement distances of 15–27 cm. The argon charge-exchange mean free path, estimated using a resonant Ar^+–Ar cross-section of $\sim 4\text{–}5\times10^{-19}\,\mathrm{m}^2$ [22], is of order 13–26 cm across the operating pressure range,

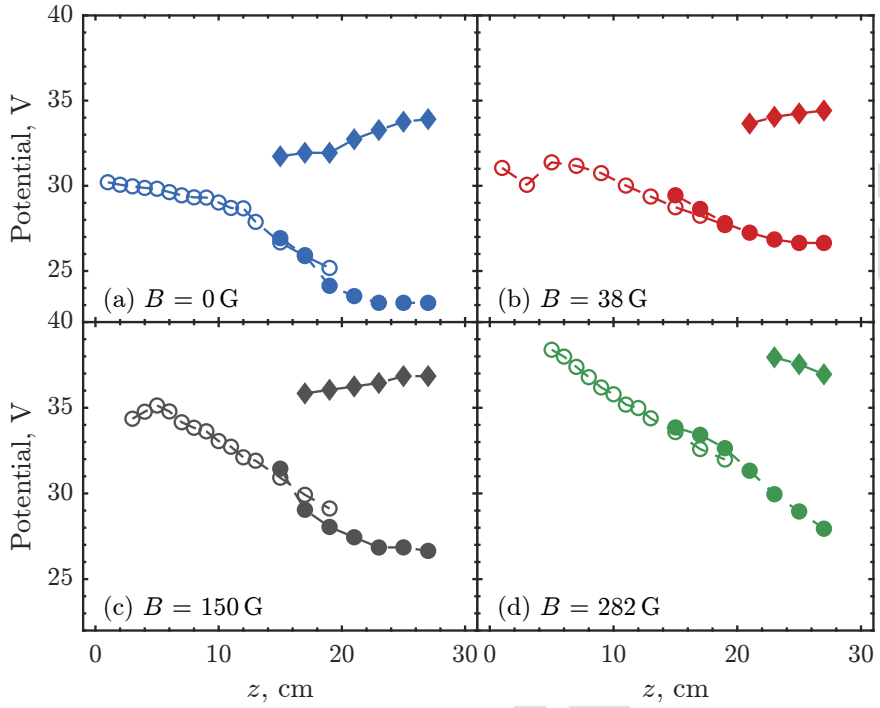


Figure 22: Axial profiles of the plasma potential (filled circles) and ion beam potential (diamonds) measured on the centreline axis for increasing magnetic field strengths $B_{z,\mathrm{max}}$. The open symbols are V_p measurements from the LP and EP, as shown in Fig. 12.

comparable to the measurement path. The beam current I_B, defined as the collector current at $V_\mathrm{D} = V_\mathrm{B}$, increases strongly with field strength (Fig. 24). At $z = 27\,\mathrm{cm}$, I_B rises from $\sim 0.02\,\mu\mathrm{A}$ at $0\,\mathrm{G}$ to $\sim 0.83\,\mu\mathrm{A}$ at $282\,\mathrm{G}$, indicating more than an order-of-magnitude increase in directed ion flux.

The approximately constant v_b together with the strong increase in I_B implies enhanced on-axis momentum delivery with increasing magnetic field strength, as discussed below.

4.7. Discussion

The results of this study demonstrate how applied axial magnetic fields fundamentally alter plasma transport, energy balance, and acceleration processes in a hollow cathode discharge operated in a low-power AF-MPDT-relevant configuration. Three key mechanisms underpin the observed behaviour:

1. **Suppression of radial transport.** As B increases, the electron Larmor radius becomes much smaller than the characteristic radial scale ($r_\mathrm{L,e} \ll L_\perp$), strongly reducing cross-field diffusion. This effect confines electrons to flux tubes, increasing residence times and enabling more efficient utilisation of the emitted electron population. The resulting density rise directly increases the ion flux.
2. **Formation of a nozzle-like potential structure.** The plasma potential adapts to the increased discharge voltage required to sustain the current under

Journal Pre-proof

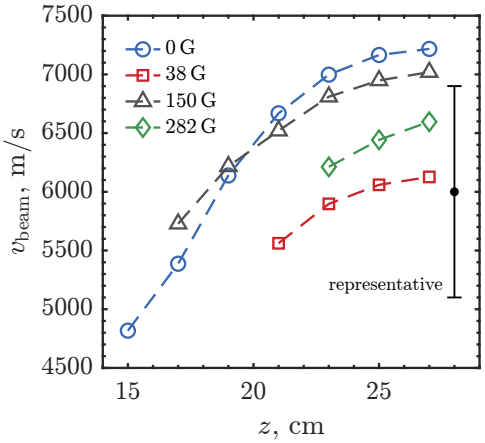


Figure 23: Ion beam speed on-axis for increasing magnetic fields. A representative error bar is shown; see Sec. 2.3 for the associated uncertainty.

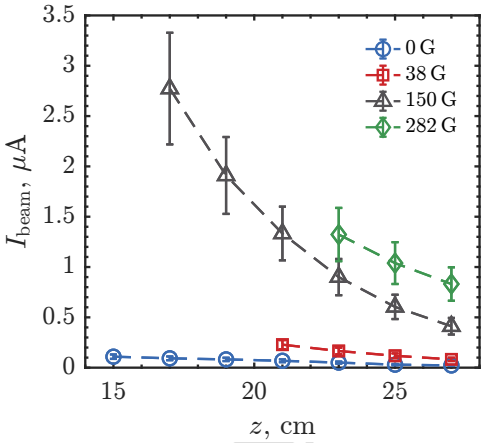


Figure 24: Ion beam current on-axis for increasing magnetic fields.

constrained cross-field transport. The resulting equipotential landscape features a strong axial gradient and inward-curving radial contours, producing both axial acceleration and radial focusing of ions.

3. **Enhanced electron heating.** The persistence of a high-energy electron population under confinement supports the hot axial core, while azimuthal $\mathbf{E} \times \mathbf{B}$ drift in regions of steep radial potential gradient is the more strongly supported mechanism for the off-axis high-temperature region observed along the outer field lines.

Together, these effects generate a denser, more energetic, and more collimated plasma jet than in the unmagnetised case. Ion-beam measurements show that the directed ion current increases strongly with magnetic field strength, even as the beam velocity remains approximately constant.

A notable trend across all measurements is the saturation behaviour at high fields. Both electron temperature and density plateau beyond $B_{z,\max} \approx 500\,\mathrm{G}$, and ion beam velocities show little variation once the nozzle-like structure is established. This suggests that the confinement-enhanced ionisation occurring near the cathode approaches a practical limit under passive magnetic shaping. Without increasing discharge current or modifying the cathode geometry, further gains in directed ion flux may not be possible. While these observations bound the gains achievable through field strength alone, the enhancement already realised relative to the unmagnetised case is substantial. To quantify it, the directed axial momentum flux carried by the on-axis ion beam can be estimated from the RPA measurements as $F_{\mathrm{ion}} = (I_{\mathrm{B}}/e)\, m_{\mathrm{Ar}}\, v_{\mathrm{b}}$. At $B_{z,\max} = 282\,\mathrm{G}$ and $z = 27\,\mathrm{cm}$, with $I_{\mathrm{B}} \approx 0.83\,\mu\mathrm{A}$, $v_{\mathrm{b}} \approx 6500\,\mathrm{m/s}$, and $m_{\mathrm{Ar}} = 6.63 \times 10^{-26}\,\mathrm{kg}$, this yields $F_{\mathrm{ion}} \approx 2.2 \pm 0.6\,\mathrm{nN}$, compared with approximately $0.06 \pm 0.01\,\mathrm{nN}$ at $0\,\mathrm{G}$, where the uncertainties combine the $\sim$20 % beam-current uncertainty (Fig. 24) and the beam-velocity uncertainty (Sec. 2.3) in quadrature. Because the beam velocity is constant to within its uncertainty across all fields

Journal Pre-proof

(Sec. 4.6), the enhancement in on-axis momentum flux is set almost entirely by the ratio of beam currents, $I_{\mathrm{B}}(282\,\mathrm{G})/I_{\mathrm{B}}(0\,\mathrm{G}) \approx 42$. Treating the beam-current uncertainties at the two field strengths as independent gives an enhancement factor of 42 ± 12 (approximately 30–54); additionally including the velocity uncertainties widens this to approximately 27–57. Under any reasonable treatment of the uncertainties, the enhancement exceeds an order of magnitude. These values are not a thrust determination: they represent the momentum flux sampled by the RPA over its acceptance area at a single on-axis location, capturing only a small fraction of the total plume momentum and, at the furthest measurement station, only after charge-exchange attenuation has reduced the directed beam. A full thrust characterisation would require a thrust balance or a spatially integrated impulse measurement. Beyond the total directed momentum, the pronounced radial collimation of the plume concentrates this flux into a smaller cross-sectional area. As the applied field increases, the density contours narrow markedly and the radial profiles sharpen (Figs. 9 and 11), so the on-axis thrust density increases more strongly with applied field than the integrated beam momentum alone. This is directly relevant to AF-MPDT operation, where thrust density and plume divergence are primary performance parameters. Together, these measurements establish that magnetic confinement produces a commensurate, quantifiable gain in on-axis momentum delivery.

Within the low-current regime examined here, these benefits support the potential viability of heaterless hollow cathodes as combined electron sources and plasma injectors for low-power AF-MPDTs.

5. Conclusions

This work has experimentally demonstrated that strong axial magnetic fields fundamentally reshape the behaviour of heaterless hollow cathode discharges operated in an AF-MPDT-relevant geometry. Spatially resolved electron and ion measurements reveal that magnetic confinement not only increases on-axis plasma density and suppresses radial transport, but also reorganises the potential field into a nozzle-like structure capable of generating a partially accelerated ion population. These effects occur at discharge currents below 10 A and without an external heater, highlighting an operational regime that has received little prior attention.

The emergence of high-energy electron populations, extended residence times, and focused potential gradients indicates that magnetic shaping can significantly enhance local energy conversion even in low-power systems. The associated increase in directed ion flux suggests a pathway for improving thrust efficiency by concentrating current density and momentum along the axis. At the same time, the observed saturation of temperature, density, and beam velocity at the highest fields points to practical limits on performance gains achievable through passive confinement alone.

Overall, the measurements establish heaterless hollow cathodes as viable plasma injectors for compact AF-MPDT concepts and provide a quantitative baseline for modelling magnetised hollow cathode behaviour in enclosed geometries. The results motivate future work incorporating higher discharge currents, upstream ionisation enhancement, and direct thrust measurements to clarify the full performance potential of this configuration and to guide the design of next-generation low-power MPD thrusters.

Journal Pre-proof

CRediT authorship contribution statement

Jakob Balkenhohl: Writing – original draft, Writing – review & editing, Conceptualization, Methodology, Validation, Formal analysis, Investigation, Data curation, Visualization. **Nicholas Rattenbury:** Supervision, Funding acquisition, Project administration, Writing – review & editing. **John Cater:** Supervision, Funding acquisition, Project administration, Writing – review & editing.

Acknowledgements

This work was supported by a New Zealand Ministry for Business Innovation and Employment (MBIE) Endeavour Fund Research Programme (MBIE Reference RTVU2003, Contract E3769).

Declaration of competing interest

The authors declare that they have no known competing financial interests or personal relationships that could have appeared to influence the work reported in this paper.

References

[1] G. P. Sutton, O. Biblarz, Rocket Propulsion Elements, ninth Edition, Wiley-VCH, 2016.

[2] R. M. Myers, Geometric Scaling of Applied-Field Magnetoplasmadynamic Thrusters, Journal of Propulsion and Power 11 (2) (1995) 343–350. doi:10.2514/3.51431.

[3] N. M. Nerheim, A. J. Kelly, A critical review of the state-of-the-art of the MPD thruster, in: 6th Electric Propulsion and Plasmadynamics Conference, Colorado Springs, CO, USA, 1967.

[4] G. Kruelle, E. Zeyfang, Preliminary conclusions of continuous applied field electromagnetic thruster research at DFVLR, in: 11th Electric Propulsion Conference, American Institute of Aeronautics and Astronautics, New Orleans, LA, U.S.A., 1975. doi:10.2514/6.1975-417.

[5] R. Pollock, J. Głowacki, M. Goddard-Winchester, S. Hellmann, X. Huang, B. Mallett, J. Olatunji, B. Pavri, C. Shellard, N. Strickland, et al., Hēki: A high temperature superconductor technology demonstration mission to the international space station, in: 2024 IEEE Aerospace Conference, IEEE, 2024, pp. 1–11.

[6] E. Bögel, M. Collier-Wright, K. Aggarwal, M. L. R. Betancourt, State of the Art Review in Superconductor-based Applied-Field Magnetoplasmadynamic Thruster Technology, in: International Electric Propulsion Conference, Boston, MA, USA, 2022.

Journal Pre-proof

[7] H. Kasuga, J. Jeong, K. Mizutani, A. Iwakawa, A. Sasoh, K. Kojima, T. Kimura, Y. Kawamata, M. Yasui, Operation Characteristics of Applied-Field Magnetoplasmadynamics Thruster Using Hollow Cathode, Transactions of the Japan Society for Aeronautical and Space Sciences, Aerospace Technology Japan 16 (1) (2018) 69–74. doi:10.2322/tastj.16.69.

[8] D. Ichihara, T. Uno, H. Kataoka, J. Jeong, A. Iwakawa, A. Sasoh, Ten-Ampere-Level, Applied-Field-Dominant Operation in Magnetoplasmadynamic Thrusters, Journal of Propulsion and Power 33 (2) (2017) 360–369. doi:10.2514/1.B36179.

[9] D. M. Goebel, I. Katz, Fundamentals of Electric Propulsion: Ion and Hall Thrusters, John Wiley & Sons (2008).

[10] D. R. Lev, I. G. Mikellides, D. Pedrini, D. M. Goebel, B. A. Jorns, M. S. McDonald, Recent progress in research and development of hollow cathodes for electric propulsion, Reviews of Modern Plasma Physics 3 (1) (2019) 6. doi:10.1007/s41614-019-0026-0.

[11] R. H. Martin, C. C. Farnell, J. Williams, Direct and remote measurements of plasma properties nearby hollow cathodes, 29th International Electric Propulsion Conference (2005).

[12] R. Martin, J. Williams, Direct Measurements of Plasma Properties nearby a Hollow Cathode Using a High Speed Electrostatic Probe, in: 42nd AIAA/ASME/SAE/ASEE Joint Propulsion Conference & Exhibit, American Institute of Aeronautics and Astronautics, Sacramento, California, 2006. doi:10.2514/6.2006-4820.

[13] R. E. Thomas, H. Kamhawi, G. J. Williams, High Current Hollow Cathode Plasma Plume Measurements, in: 33rd International Electric Propulsion Conference, Washington D.C., 2013.

[14] J. Balkenhohl, N. Rattenbury, J. Cater, An Experimental Setup for the Performance Analysis of Low-Power Hollow Cathodes at High Applied Magnetic Field Strengths, in: Proceedings of the Aerospace Europe Conference 2023 - 10th EUCASS - 9th CEAS, 2023, p. 535. doi:10.13009/EUCASS2023-535.

[15] M. J. Druyvesteyn, Der Niedervoltbogen, Zeitschrift für Physik 64 (11-12) (1930) 781–798. doi:10.1007/BF01773007.

[16] V. I. Demidov, S. V. Ratynskaia, R. J. Armstrong, K. Rypdal, Probe measurements of electron energy distributions in a strongly magnetized low-pressure helium plasma, Physics of Plasmas 6 (1) (1999) 350–358. doi:10.1063/1.873288.

[17] G. Becatti, R. W. Conversano, D. M. Goebel, Demonstration of 25,000 ignitions on a proto-flight compact heaterless lanthanum hexaboride hollow cathode, Acta Astronautica 178 (2021) 181–191. doi:10.1016/j.actaastro.2020.09.013.

[18] R. Joussot, L. Grimaud, S. Mazouffre, Examination of a 5 A-class cathode with a LaB6 flat disk emitter in the 2 A–20 A current range, Vacuum 146 (2017) 52–62. doi:10.1016/j.vacuum.2017.09.021.

Journal Pre-proof

[19] A. Boschi, F. Magistrelli, Effect of a R.F. signal on the characteristic of a langmuir probe, Il Nuovo Cimento 29 (2) (1963) 487–499. doi:10.1007/bf02750367.

[20] H. Sabadil, S. Klagge, M. Kammeyer, Langmuir probe measurements of axial variation of plasma parameters in 27.1 MHz RF oxygen planar discharges, Plasma Chemistry and Plasma Processing 8 (4) (1988) 425–444. doi:10.1007/bf01016058.

[21] J. M. Hoell, D. R. Brooks, Distribution of plasma potential for an MPD thruster, AIAA Journal 6 (4) (1968) 723–725. doi:10.2514/3.4572.

[22] D. Rapp, W. E. Francis, Charge exchange between gaseous ions and atoms, The Journal of Chemical Physics 37 (11) (1962) 2631–2645. doi:10.1063/1.1733066.

Journal Pre-proof

Journal Pre-proof

- Spatially resolved EEPF and IEDF diagnostics of a heaterless hollow cathode plasma
- Axial magnetic fields up to 800 G strongly increase on-axis plasma density
- Nozzle-like plasma potential structure promotes axial ion acceleration
- Emergence of a magnetically confined beam-like ion population
- Results support heaterless cathodes as injectors for low-power AF-MPDT concepts

Journal Pre-proof

Journal Pre-proof

Declaration of interests

☒ The authors declare that they have no known competing financial interests or personal relationships that could have appeared to influence the work reported in this paper.

☐ The authors declare the following financial interests/personal relationships which may be considered as potential competing interests:

Journal Pre-proof